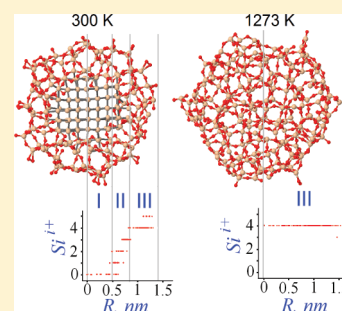


## Self-Limiting Oxidation in Small-Diameter Si Nanowires

U. Khalilov,<sup>\*,†</sup> G. Pourtois,<sup>‡,‡</sup> A. C. T. van Duin,<sup>§</sup> and E. C. Neyts<sup>†</sup><sup>†</sup>Department of Chemistry, PLASMANT Research Group, University of Antwerp, Universiteitsplein 1, B-2610 Wilrijk-Antwerp, Belgium<sup>‡</sup>IMEC, Kapeldreef 75, B-3001 Leuven, Belgium<sup>§</sup>Department of Mechanical and Nuclear Engineering, Penn State University, University Park, Pennsylvania 16802, United States

**ABSTRACT:** Recently, core shell silicon nanowires (Si-NWs) have been envisaged to be used for field-effect transistors and photovoltaic applications. In spite of the constant downsizing of such devices, the formation of ultrasmall diameter core-shell Si-NWs currently remains entirely unexplored. We report here on the modeling of the formation of such core shell Si-NWs using a dry thermal oxidation of 2 nm diameter (100) Si nanowires at 300 and 1273 K, by means of reactive molecular dynamics simulations using the ReaxFF potential. Two different oxidation mechanisms are discussed, namely a self-limiting process that occurs at low temperature (300 K), resulting in a Si core | ultrathin SiO<sub>2</sub> silica shell nanowire, and a complete oxidation process that takes place at a higher temperature (1273 K), resulting in the formation of an ultrathin SiO<sub>2</sub> silica nanowire. The oxidation kinetics of both cases and the resulting structures are analyzed in detail. Our results demonstrate that precise control over the Si-core radius of such NWs and the SiO<sub>x</sub> ( $x \leq 2.0$ ) oxide shell is possible by controlling the growth temperature used during the oxidation process.

**KEYWORDS:** Si nanowires, self-limiting oxidation, molecular dynamics, simulation



## ■ INTRODUCTION

In the past decade, the interest in silicon nanowires (Si-NWs) has increased tremendously, as they are being used extensively in nanoscale electronic devices,<sup>1,2</sup> including nanowire field-effect transistors (FET), thin film transistors,<sup>1–5</sup> photo-detectors, thin-film solar cells,<sup>6</sup> and nanowire-based electrochemical biosensors.<sup>7</sup> Therefore, several growth methods of Si-NWs have been reported, analyzing general aspects of their growth.<sup>8</sup> Small-diameter Si nanowires in particular are potentially very attractive because of the possibility to exploit quantization of the electronic structure. As demonstrated by Ma and co-workers,<sup>3</sup> the band gap of Si-NW can be increased by reducing their diameter to less than 3 nm. This indicates the possibility of developing Si-NW with a controllable band gap. Similarly, theoretical considerations suggest that an enhancement of the radiative transitions is occurring due to quantization when their physical dimensions lie below 5 nm.<sup>9</sup> As a result of these very appealing observations, different methods have been developed for their fabrication with controlled small diameters.<sup>3</sup> Usually, small diameter Si-NWs are obtained by oxidizing the larger ones and by subsequently removing the formed oxide layer.<sup>10</sup> The mechanisms of oxidation of small diameter nanowires are therefore also being studied extensively.<sup>5,10–13</sup> Since the Deal-Grove model<sup>14</sup> only considers the oxidation of planar bulk silicon, some modifications need to be applied for describing two-dimensional (cylindrical) structures, as outlined in detail for wet oxidation by Kao et al.<sup>15</sup> The mechanism of the initial oxide growth, however, cannot be properly explained with this

model.<sup>11</sup> Furthermore, self-limiting oxidation of small diameter Si-NWs has not yet been properly investigated.

Self-limiting oxidation of Si nanowires and spheres is of considerable concern, for instance for the design of metal-oxide-semiconductor (MOS) devices<sup>4,5,15</sup> or photovoltaic cells.<sup>6</sup> The early work on self-limiting oxidation performed by Liu et al.<sup>16</sup> analyzed the dry thermal oxidation of Si-NWs starting from an initial diameter of  $\sim 30$  nm. They suggested that the final Si core diameter can be controlled by the oxidation temperature. Self-limiting oxidation was also explained by a retarded oxidation process of Si nanowires.<sup>11</sup> It was found that such an oxidation behavior strongly depends on the nanowire curvature, the sign of curvature (i.e., convex or concave shape) and the growth temperature. Various modeling efforts and analyses regarding this effect can be found elsewhere.<sup>5,10,11,13,17–19</sup> However, all conclusions were related to Si-NWs with diameters above 3 nm and higher temperatures, i.e., starting from 600 °C.

Because of the interesting properties of small diameter ( $< 3$  nm) Si NWs, as outlined above, careful studies are needed to unravel their oxidation mechanisms at the atomic scale. This paper is therefore focused on the oxidation behavior of such small diameter NWs as a function of the oxidation temperature. We report here on the oxidation process and structure analysis of oxygenated Si-NWs with initial diameter of 2 nm at

Received: March 5, 2012

Revised: May 16, 2012

Published: May 18, 2012

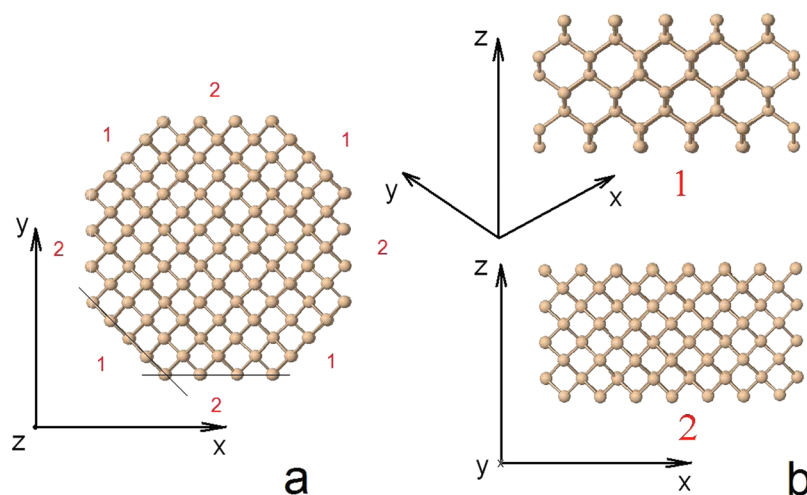


**Figure 1.** Ideal structure of Si nanowires (Si-NWs) with 2 nm diameter: (a) top and (b) side view. Here, 1 and 2 indicate  $\{110\}$  and  $\{001\}$ -type facets, respectively.

temperatures of 300 and 1273 K, studied by means of reactive molecular dynamics simulations using the ReaxFF potential.

## ■ COMPUTATIONAL DETAILS

**1. Interatomic Potential.** The growth process of  $\text{SiO}_2$  during the thermal oxidation of Si NWs at the atomic scale is studied by reactive MD simulations. Forces on the atoms are derived from the reactive force field (ReaxFF) potential, which was developed by van Duin et al.<sup>20</sup> The potential uses the bond order/bond distance relationship formally introduced by Abell.<sup>21</sup> Overcoordination and undercoordination energy penalties are used to enforce the correct bond order. The total system energy is the sum of several partial energy terms related to lone pairs, undercoordination, overcoordination, valence, and torsion angles, conjugation, hydrogen bonding, as well as van der Waals and Coulomb interactions. The ReaxFF potential can describe both covalent and ionic bonds, as well as the entire range of intermediate interactions. Charge distributions are calculated using the electronegativity equalization method (EEM), based on the system geometry and connectivity.<sup>22</sup> The EEM parameters were fitted against Mulliken charge distribution. In this work, we use the force field parameters employed by Buehler et al.<sup>23</sup> This force field was trained extensively against both Si and  $\text{SiO}_2$  phases. Although  $\text{SiO}_x$  ( $x < 2.0$ ) suboxide phases were not included explicitly in this training, our previous results on a planar  $\text{Si/SiO}_2$  interface including these Si suboxide species were in agreement with both experimental and DFT results.<sup>24</sup> A detailed description of the force field can be found elsewhere.<sup>23–26</sup> Currently, the ReaxFF potential can successfully describe tens of elements and their compounds, including hydrocarbons, silicon/silicon oxide,<sup>24,27–29</sup> metals and metal-catalyzed reactions,<sup>30,31</sup> metal oxides,<sup>32</sup> metal hydrides,<sup>33</sup> and others.

**2. Simulation Methodology.** Si(100) nanowires with diameter of 2 nm and of 1 nm length are considered. In figure 1a, the ideal Si(100) nanowire structure at 0 K is shown. A periodic boundary condition is applied along the  $z$ -direction, which corresponds to the axial direction of the nanowire, in order to mimic an infinitely long nanowire. The nanowire is terminated by four  $\{110\}$ -type and four  $\{001\}$ -type facets (denoted by 1 and 2, respectively in Figure 1). The angle between two  $\{110\}$  or two  $\{001\}$ -type facets is  $90^\circ$ , whereas the one between two  $\{110\}$  and  $\{001\}$  facets is  $135^\circ$ .

Prior to oxidation, the octagon-shaped Si(100) NWs are equilibrated at 300 and 1273 K using the Berendsen thermostat and barostat (NpT ensemble)<sup>34</sup> for 40 ps with temperature and pressure damping constants of 0.1 and 5.0 ps, respectively. The obtained structures are subsequently relaxed in the microcanonical NVE ensemble for 20 ps. After thermalization, the structure as obtained at low temperature (300 K) almost keeps the same shape, displaying both facets, similar to the ideal sample (see figure 2a). It was suggested

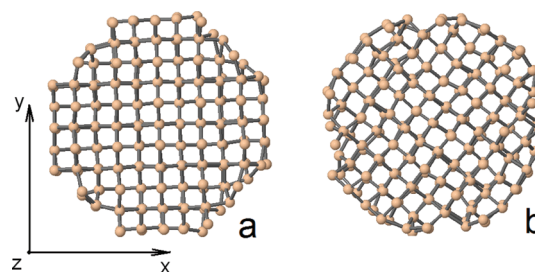


**Figure 2.** Initial structures after thermalization at (a) 300 K and (b) 1273 K, respectively.

that such faceting affects the surface reaction coefficient and subsequently the oxidation rate as well.<sup>10,12,15,18</sup> At high temperature (1273 K), however, the shape of the NW structure becomes circular (see figure 2b).

Both obtained structures are analyzed by the radial distribution function (RDF). The RDF shows that the first, second, third and fourth neighbors of Si atoms are located at 0.23, 0.38, 0.44, and 0.53 nm, respectively. The Si–Si–Si peak in the angle distribution corresponds to about  $110^\circ$ . These parameters are close to the experimental values for Si(100) NWs.<sup>3</sup>

Oxygen impacts are performed as follows. Each incident oxygen molecule is positioned at 1 nm above the uppermost atom of the nanowire in the  $(x,y)$  plane. The  $z$  coordinates of the incident particles are chosen randomly. The  $\text{O}_2$  molecule is rotated randomly prior to impact. Every impact is followed for 10 ps, after which the next impact starts. The initial velocity vector of the incident molecule is randomized and its magnitude is set to the root-mean-square velocity corresponding to the oxidation temperature. During the impacts, NpT dynamics are applied to mimic dissipation of the heat of reaction and to allow for a volume expansion due to the oxidation process. In total, 2240 and 1456 consecutive impacts were performed at 300 and 1273 K, respectively.

## ■ RESULTS AND DISCUSSION

**1. Oxidation and Oxide Growth Process.** The thermalized Si-NWs are oxidized by  $\text{O}_2$  molecules at 300 and 1273 K. Figure 3 presents general information on the oxidation and the (sub)oxide growth process on Si-NWs with diameter of 2 nm, at low (300 K) and high (1273 K) temperature. The figure shows the evolution of the oxygen content (right axis), oxide shell thickness, radii of the Si-core and total oxygenated Si-NW (left axis) as a function of the  $\text{O}_2$  fluence in monolayers

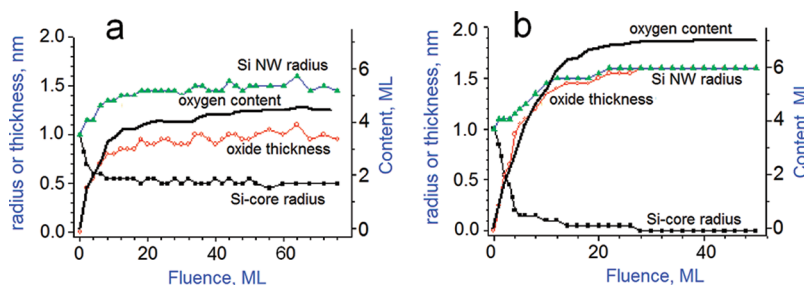


**Figure 3.** Evolution of the oxide shell and Si-core thickness, and total Si NW radius (left axis), as well as oxygen content (right axis) during oxidation of a Si-NW with initial diameter of 2 nm at (a) 300 K and (b) 1273 K.

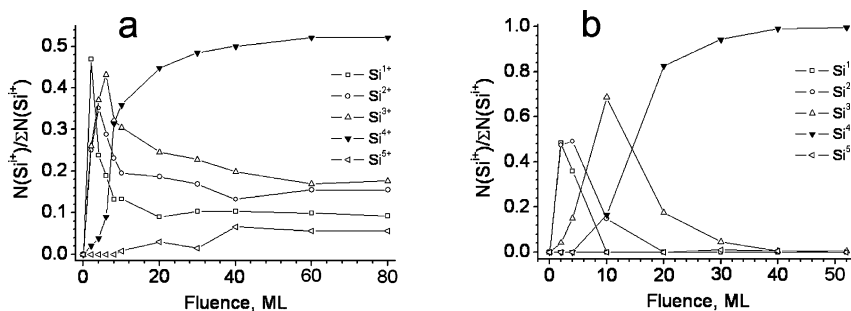


**Figure 4.** Variation in the fraction of Si-suboxide components during oxidation at (a) 300 K and (b) 1273 K.

(ML) for both temperatures. In these calculations, one ML corresponds to 56 atoms. At 300 K (Figure 3a), the oxide growth process saturates after 60 ML, resulting in an oxide thickness of 1 nm. At the same time, the Si-core radius drops from 1 to 0.5 nm, and consequently, the total Si-NW radius increases to 1.5 nm. The oxygen content after saturation is about 4.5 ML. At 1273 K (Figure 3b), on the other hand, the Si-NW is completely oxidized after 40 ML.

At both temperatures, the oxidation appears to change from a linear to a logarithmic function of time. Such oxidation behavior corresponds roughly to the Deal–Grove theory for planar Si.<sup>14</sup> Kao and co-workers<sup>15</sup> presented an extension of the Deal–Grove model for the wet oxidation of cylindrical Si (or Si-NW), applying the following equation to describe the kinetics of the process at the SiSiO<sub>2</sub> interface:

$$\frac{\partial x}{\partial t} = \frac{1}{N} \frac{C^*}{\frac{1}{k_s} + \frac{1}{h} \frac{a}{b} + \frac{1}{D} \log\left(\frac{b}{a}\right)} \quad (1)$$

where  $N$  is the number of oxidants required to form a cubic unit of oxide,  $a$  is the NW core radius,  $b$  is the total NW radius (Si core + SiO<sub>2</sub> shell), and  $x = b - a$  is the oxide thickness. It is assumed that the oxide growth rate is determined by the surface reaction rate coefficient  $k_s$  at the SiO<sub>2</sub>|Si interface, the surface mass transfer constant  $h$  of the oxidant, the diffusivity  $D$  of the oxidant in SiO<sub>2</sub>, and the solid solubility  $C^*$  of the oxidant in SiO<sub>2</sub>.

However, this equation should be altered for oxidation of the pure Si NW, i.e., in the initial oxidation stage. In this stage, the  $(1/D)\log(b/a)$  term is omitted as  $a$  and  $b$  are initially equal to 1.0 nm. Generally, the  $1/D$  and  $1/h$  terms are included for oxidation of Si with a pre-existing oxide layer (i.e.,  $b > a$ ) and they should be ignored in the initial oxidation stage. The parameter  $C^*$ , which equals the oxygen flux (or oxygen fluence) is constant in this stage. As a result, the oxidation rate depends only on the surface reaction coefficient in the initial oxidation stage. As suggested in<sup>15,24</sup> for planar oxidation, the growth rate

is determined by the surface reaction rate coefficient  $k_s$  for thinner oxides, i.e.,  $x_o \approx 0$ . The  $k_s$  parameter depends on the initial surface reaction rate coefficient ( $k_{s0}$ ), the normal stress ( $\sigma$ ) and the surface temperature ( $T$ ).<sup>15</sup> However, in the initial oxidation stage, the surface reaction coefficient strongly depends on  $k_{s0}$  rather than on the stress and oxidation temperature. We calculated stresses as the symmetric per-atom stress tensor for each atom in the Si-NW using the approach proposed in reference.<sup>35</sup> The tensor has 6 components for each atom and is stored as a 6-element vector in rectangular Cartesian coordinates:  $\sigma_{xx}, \sigma_{yy}, \sigma_{zz}, \sigma_{yz}, \sigma_{zx}, \sigma_{xy}$  and correspondingly in cylindrical coordinates  $\sigma_{rr}, \sigma_{\theta\theta}, \sigma_{zz}, \sigma_{\theta z}, \sigma_{zr}, \sigma_{r\theta}$ . The stress components in all directions are averaged per unit radius of 0.232 nm, which corresponds to the distance between first Si–Si neighbors in the crystalline Si-NW. The calculations show that the radial (normal,  $\sigma_{rr}$ ) and tangential ( $\sigma_{\theta\theta}$ ) stresses on a nonoxidized Si-NW surface are compressive and relatively small, i.e.,  $\sigma_{rr} \sim 0.2$  GPa and  $\sigma_{\theta\theta} \sim 0.03$  GPa. Kao et al.<sup>15</sup> suggested that  $\sigma_{rr}$  and  $\sigma_{\theta\theta}$  components are almost zero in a pure cylindrical Si. Although the axial stress is somewhat higher ( $\sigma_{zz} \approx 0.3$  GPa), due to the periodic boundary in the  $z$ -direction, we believe that the reaction rate coefficient is not significantly lowered by the stress in the initial oxidation stage. As a result, the initial oxidation rate depends more strongly on the stress-free initial reaction rate coefficient rather than on stress and temperature. Therefore, as shown in figure 3, the oxide thickness quickly increases during the initial oxidation stage, due to the initial reaction rate, which depends on the surface crystallographic orientation, the number of dangling bonds on the nanowire surface, and the surface energy barrier. Note that the sticking behavior also depends on the spin-state, i.e., singlet or triplet state of an incident O<sub>2</sub> molecule,<sup>37,38</sup> which is not taken into account in our calculations. ReaxFF does not include the concept of multiple spin states and is parametrized to reproduce the energy corresponding to the lowest energy spin state. Therefore, in our simulations, the spin state corresponding to the lowest-energy path is assumed at all times.

The time evolution of the formation and growth of the oxygenated silicon in the initial stage of planar surface oxidation can easily be understood by observing the variation of the silicon suboxide components, i.e.,  $\text{Si}^{1+}$ ,  $\text{Si}^{2+}$ ,  $\text{Si}^{3+}$ , and  $\text{Si}^{4+}$ , which bind to one, two, three, and four nearest-neighbor oxygen atoms, respectively.<sup>38</sup> The notation used corresponds to formal charge states and not to actual atomic charges. As shown in Figure 4, all four Si suboxide species are found in Si-NW oxidation as well. Also some overcoordinated silicon, i.e., 5-fold suboxide ( $\text{Si}^{5+}$ ) species are detected on the silica surface, although in low concentration. Initially, only  $\text{Si}^{1+}$  and  $\text{Si}^{2+}$  are formed. As the oxidation progresses, these are transformed into  $\text{Si}^{3+}$  and subsequently into  $\text{Si}^{4+}$ . The  $\text{Si}^{1+}$ ,  $\text{Si}^{2+}$ , and  $\text{Si}^{3+}$  fractions consecutively dominate in the initial oxidation stage (see Figure 4). Usually, such an oxidation behavior is also observed in the oxidation of planar Si.<sup>24,39</sup> When a stoichiometric oxide layer appears, the fraction of  $\text{Si}^{4+}$  components increases continuously and the one of the other suboxide components decreases. It is only in the final oxidized wire step, at high temperature, that all Si atoms are converted in the  $\text{Si}^{4+}$  oxidation state (Figure 4b). On the other hand, at low temperature, all Si-suboxide components can be found in the final structure, as is illustrated from Figure 4a.

The oxidation is continued until the oxygen content saturates. At high temperature, the saturation occurs faster (see Figures 3 and 4) because of the relatively high diffusivity and mobility of the oxidant, i.e., the oxide thickness also depends on the diffusion coefficient  $D$  (see eq 1). Therefore, the Si-core radius ( $a$ ) goes to zero during thermal dry oxidation at high temperature (see Figure 3a). This indicates that the Si-NW completely converts to a  $\text{SiO}_2$ -NW, as is also shown in Figure 4b, where the  $\text{Si}^{4+}$  fraction becomes equal to 1. At low temperature, however, the Si-core radius shrinks down to about 0.5 nm after which, it remains constant. On the other hand, the contribution of long time scale diffusion to eq 1 cannot be accurately accounted for in MD simulations. As a result, the partially oxidized structure may finally become fully oxidized, provided a sufficiently long oxidation time (in the range  $1 \times 10^3$  to  $1 \times 10^5$  s depending on the experimental conditions in planar surface oxidation<sup>39</sup>) is permitted at 300 K. However, the final structure can be analyzed without including the long time scale contribution by means of the following theoretical approach,<sup>19</sup> with which also most experimentalists compare their results<sup>5,10,11</sup>

$$(b^2 - a^2)L - \pi(b_0^2 - a_0^2)L = k\pi(a_0^2 - a^2)L \quad (2)$$

where  $a_0$  and  $a$  are the initial and final radii of the Si core, respectively,  $b_0$  and  $b$  are the initial and final radii of the Si-NW, respectively,  $L$  is the Si-NW length, and  $k$  is a coefficient. This coefficient  $k$  indicates that the molecular volume of  $\text{SiO}_2$  ( $\sim 45 \text{ \AA}^3$ ) is about 2.25 times larger than the atomic volume of Si ( $20 \text{ \AA}^3$ ).<sup>10–12,15,17</sup> From eq 2, the following formula including this initial condition (i.e.,  $a_0 = b_0$ ) can be obtained:

$$\frac{b}{a} = \sqrt{2.25 \frac{a_0^2}{a^2} - 1.25} \quad (3)$$

Applying eq 3 to our 300 K case, we find  $b/a \approx 2.7$ . In our MD calculation, this ratio is about 2.9, which is indeed very close to the theoretical prediction. Indeed, in this case, the oxidation process does not depend on the diffusion coefficient and is only function of the surface reaction rate, which depends on the normal stress rather than on the temperature. It has been

suggested (see e.g., refs 15–18) that such compressive stresses at the  $\text{Si}/\text{SiO}_2$  interface significantly slow down the reaction rate. Furthermore, a compressive pressure in  $\text{SiO}_2$  reduces the oxidant diffusion and concentration. The oxidation is therefore self-limiting. Note that this behavior is not unique to Si-NWs, but is also observed in the hyperthermal oxidation of planar Si surfaces with the formation of a thin oxide surface layer at room temperature.<sup>23,24</sup> Although the current work is dedicated to a morphological analysis of the obtained structures, a detailed analysis regarding the stress and pressure evolutions during the oxidation process will be presented in a forthcoming publication.

**2. Analysis of the Obtained Structures.** At the end of the oxidation process, two different structures, i.e., silicon–silica ( $\text{Si}/\text{SiO}_x/\text{SiO}_2$ ) and pure silica ( $\text{SiO}_2$ ) are obtained at 300 and 1273 K, respectively, as shown in Figure 5a. As mentioned in

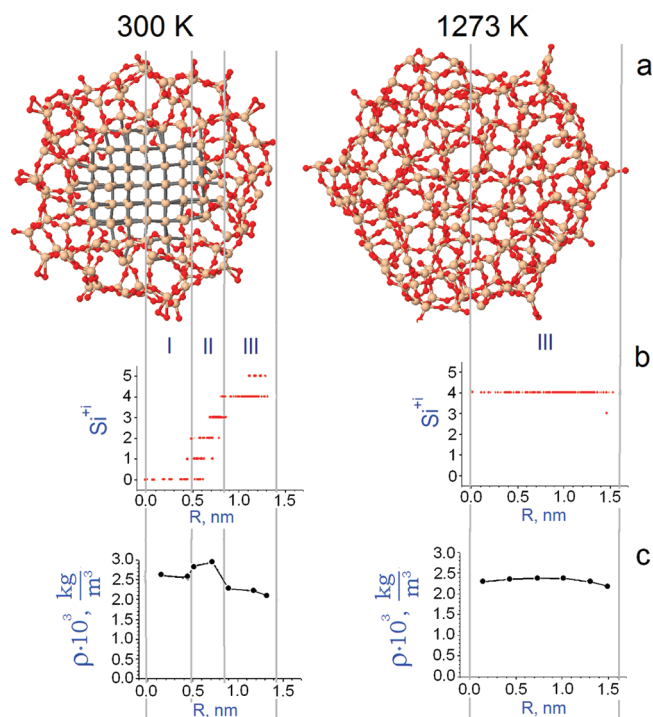


**Figure 5.** Analysis of (a) postoxidation structures obtained at 300 and 1273 K by (b) their Si-suboxide components and (c) their mass density distribution.

the previous section, the formation of such a structure at low temperature can be explained by self-limiting oxidation.<sup>15,16</sup> In contrast to the oxidation at low temperature, the Si-NW is completely oxidized at high temperature (1273 K), in agreement with the experimental observations reported by Büttner and Zacharias.<sup>11</sup> They found that 925 °C ( $\sim 1200$  K) is a sufficient temperature for complete oxidation of a Si-NW with an initial radius of 15 nm or less. Since the molecular volume of  $\text{SiO}_2$  ( $45 \text{ \AA}^3$ ) is larger than the atomic one of Si ( $20 \text{ \AA}^3$ ), the newly formed oxide continuously pushes the 'old' oxide outward, in order to accommodate the volume expansion.<sup>11,16</sup> As a result, the final diameters of both structures are found to be 2.9 and 3.1 nm at 300 and 1273 K, respectively, at the end of the oxidation process. This corresponds to an expansion by a factor of 2.1 and 2.4 relative to the initial dimensions of the Si-NWs. Note that the expansion coefficient of 2.4 as obtained at a high temperature treatment is larger than the ideal expansion

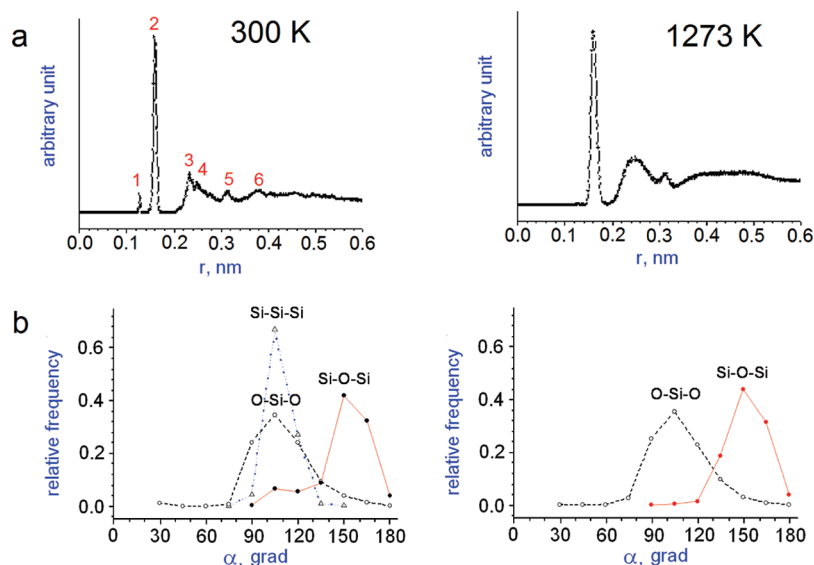


**Figure 6.** Analysis of the obtained Si-core and SiO<sub>2</sub> structures by means of (a) radial distribution function and (b) angle distribution at 300 and 1273 K.

one obtained for Si-to-SiO<sub>2</sub> (2.25),<sup>10–12,15,17</sup> since in the current oxidation process, a low density amorphous SiO<sub>2</sub> phase is formed rather than the high density quartz one.

As shown in Figure 5b, both obtained structures are analyzed by the distribution in their suboxide components. The distribution of the Si-suboxide components in the oxidized Si-NW at 300 K shows that the final structure contains three regions, i.e., region I corresponds to a Si-core region (containing only Si<sup>0</sup>), region II to a SiSiO<sub>2</sub> interface (existing of Si<sup>1+</sup>, Si<sup>2+</sup>, Si<sup>3+</sup>) and region III to an ultrathin SiO<sub>2</sub> shell (consisting of Si<sup>4+</sup>). At high temperature, the distribution of Si<sup>4+</sup> indicates that the Si structure completely converts to silica (SiO<sub>2</sub>).

As can be seen in Figure 5c, the mass density of the structure obtained at high temperature is around 2250 kg/m<sup>3</sup>, which is close to the value for amorphous silica.<sup>28</sup> The surface density is however slightly lower. In the structure obtained at low temperature, the mass density of the Si core is about 2550 kg/m<sup>3</sup>. Since the experimental silicon density is about 2330 kg/m<sup>3</sup> at room temperature, the silicon density in our calculations is slightly too high in the low temperature regime. Indeed, differences with the experiment of this order are virtually inevitable in force field generated structures. In the SiSiO<sub>2</sub> interface, where most of the intermediate Si-suboxide components (Si<sup>1+</sup>, Si<sup>2+</sup>, Si<sup>3+</sup>) reside, a relatively high mass density is found. As a matter of fact, the entering oxygen atoms are stopped by the silicon energy barrier (cf. the planar oxidation case<sup>24,29,36</sup>) such that the interface region is enriched in oxygen. Finally, in the SiO<sub>2</sub> shell at low temperature, the mass density was found to be slightly lower than the mass density of the silica obtained at high temperature due to the occurrence of a small number of O–O peroxy bridges.<sup>40</sup>

Both structures are also analyzed by means of their radial distribution functions (RDF), as shown in figure 6a. For the model formed at high temperature, three peaks are found. These three peaks correspond to the Si–O bond, nonbonded O–O and Si–Si neighbor distances, located at 0.16, 0.25, and 0.32 nm, respectively. These values agree with both experimental and other MD reports,<sup>28,41,42</sup> and indicate that the obtained structure is indeed amorphous silica. However, at

low temperature, the number of peaks increases up to six because of the occurrence of the three different aforementioned regions in the obtained structure, i.e., the crystalline Si-core, the SiSiO<sub>2</sub> interface and the ultrathin SiO<sub>2</sub> layer. The first peak, located at 0.13 nm, indicates that the silica surface contains a number of O–O peroxy bonds,<sup>40</sup> which also play a role in the appearance of Si<sup>5+</sup> on the oxygenated Si-NW surface. A similar effect was also suggested by DFT calculations analyzing various defects during planar Si oxidation.<sup>43,44</sup> The formation of an intermediate structure in which the extra oxygen atom is attached to the shared Si atom and acts as its fifth neighbor was proposed. The process then becomes a three-step mechanism. It begins with the formation of a peroxy bridge, then evolves into a 5-fold Si configuration, and finally leads to the formation of a new peroxy bridge connected to another Si atom. The appearance of the peroxy bridge bonds reduces the silica mass density as mentioned above, which explains the slightly lower mass density of the silica obtained at low temperature (see figure 5c). The second peak, located at about 0.16 nm, corresponds to Si–O bonds in the silica. This bond length is close to the Si–O one in the high temperature silica, although the peak is narrower due to the thermal widening at high temperature. The third and sixth peaks correspond to the Si–Si first (0.23 nm) and second (0.38 nm) nearest-neighbors, respectively, in the Si-core. Other near-neighbor interactions almost completely disappeared due to the oxidation. Finally, the fourth and fifth peaks of the RDF are related to O–O (0.25 nm) and Si–Si (0.32 nm) nonbonded interactions, respectively, in the ultrathin silica. The RDF analyses indicate that the obtained silica structures are amorphous at both temperatures.

Figure 6b shows the angle distributions in both structures. The Si–Si–Si angle distribution characterizes the non-oxygenated Si, and is therefore only present in the structure obtained at low temperature (due to the presence of the Si-core). The peak in the Si–Si–Si distribution is about 110°, which is close to the peak of the pure Si-NW one, as mentioned above. The oxygenated Si region is characterized by the Si–O–Si and O–Si–O angles. For both structures, most O–Si–O angles are distributed around 110° which corresponds to the tetrahedral silicon and silica structures. In  $\alpha$ -quartz, this angle is

the tetrahedral angle of  $109.5^\circ$ . The peaks are slightly wider in our structures (i.e.,  $75\text{--}165^\circ$ ) than the O–Si–O angle distribution usually cited for amorphous silica (i.e.,  $109^\circ \pm 10^\circ$ ).<sup>28,42,45</sup> Also, for the structure obtained at low temperature, an additional feature is found around  $30^\circ$ , which corresponds to the O–Si–O angle formed by some intrinsic defects, i.e., oxygen peroxy bonds on the silica surface.

The amorphous silica structure is further characterized by the Si–O–Si angles, i.e., both by its peak position and the distribution range of this angle. For comparison, the Si–O–Si angle in  $\alpha$ -quartz is  $144^\circ$ . In the case of amorphous silica, slightly differing mean values of the Si–O–Si angle distribution have previously been reported. Mozzi and Warren<sup>42</sup> obtained for the vitreous (amorphous) silica structure, which is generated by thermal O<sub>2</sub> oxidation, a wide distribution of Si–O–Si angles varying between  $120^\circ$  and  $180^\circ$ , with a main peak found at  $144^\circ$ . Watanabe et al.<sup>46</sup> investigated the thermal growth process using large-scale molecular dynamics and concluded that the Si–O–Si bond angle present in ultrathin SiO<sub>2</sub> film is reduced from  $144^\circ$  toward  $130^\circ$  to  $140^\circ$ . However, Da Silva et al.<sup>47</sup> suggested that the most probable Si–O–Si bond angle of vitreous silica is  $152^\circ$  instead of  $144^\circ$ . Mauri et al.<sup>45</sup> also found a slightly higher mean value of  $151^\circ \pm 11^\circ$  and a relatively narrow distribution ( $120\text{--}170^\circ$ ) in the Si–O–Si angular distribution of vitreous silica. In our high temperature model, the Si–O–Si angle distribution is in the range of  $120\text{--}180^\circ$ , peaking at  $\sim 150^\circ$ . These values are in fairly good agreement with the results obtained from thermal O<sub>2</sub> oxidation of a flat Si surface,<sup>47</sup> and in very good agreement with the DFT results of Mauri et al.<sup>45</sup> However, in the structure obtained at low temperature, the total Si–O–Si distribution is somewhat wider ( $90\text{--}180^\circ$ ), with a peak located at about  $150^\circ$ . The lower angle part of this distribution is due to the strain build-up near the interface, which corresponds to a distribution in the range of  $90\text{--}125^\circ$ . At low temperature, the overall spread in the RDF, angle, and mass density distributions confirms that the obtained structure consists of a crystalline Si region, an ultrathin SiSiO<sub>2</sub> interface and an amorphous SiO<sub>2</sub> shell, although some intrinsic defects, i.e., some oxygen peroxy bridge bonds, are found in the silica region. Therefore, all Si-suboxide components (Si<sup>*i*+</sup>, *i* ≤ 4) can be found in the structure obtained at low temperature. Also, some overcoordinated Si atoms (Si<sup>5+</sup>) exist on the surface of this structure as mentioned before. At high temperature, the crystalline Si-NW converts completely to an amorphous silica (*a*-SiO<sub>2</sub>) nanowire.

## CONCLUSION

Thermal oxidation of Si-NWs with a diameter of 2 nm was studied at two different temperatures (300 and 1273 K) by reactive MD simulations. The oxidation mechanism was found to be temperature dependent. After oxidation, two types of nanostructures were obtained: ultrathin SiO<sub>2</sub> silica (i.e., dielectric) nanowire at high temperature, and a Si core | ultrathin SiO<sub>2</sub> silica shell (i.e., semiconductor + dielectric) nanowire at low temperature. The Si-core radius and the SiO<sub>*x*</sub> (*x* ≤ 2.0) oxide shell can be accurately controlled in the nanoscale regime by controlling the oxidation temperature. The obtained structures were analyzed by the radial distribution function, their mass density and their angle distributions. The overall analyses show that both ultrathin silica structures are amorphous, albeit some intrinsic defects were found in the structure formed at room temperature.

## AUTHOR INFORMATION

### Corresponding Author

\*E-mail: umedjon.khalilov@ua.ac.be.

### Notes

The authors declare no competing financial interest.

## ACKNOWLEDGMENTS

U.K. acknowledges imec for financial support. A.C.T.v.D. acknowledges funding from the Air Force Office of Scientific Research (AFOSR) under Grant FA9550-10-1-0563. The authors also gratefully acknowledge financial support from the Prime Minister's Office through IAP VI. This work was carried out using the Turing HPC infrastructure at the CalcUA core facility of the Universiteit Antwerpen (UA), a division of the Flemish Supercomputer Center VSC, funded by the Hercules Foundation, the Flemish Government (department EWI) and the UA. Finally, the authors also thank Prof. A. Bogaerts for the useful discussions.

## REFERENCES

- (1) Hayden, O.; Agarwal, R.; Lu, W. *Nanotoday* **2008**, *3*, 5–6.
- (2) Bandaru, P. R.; Pichanusakorn, P. *Semicond. Sci. Technol.* **2010**, *25*, 024003.
- (3) Ma, D. D. D.; Lee, C. S.; Au, F. C. K.; Tong, S. Y.; Lee, S. T. *Science* **2003**, *299*, 1874 and references therein.
- (4) Trivedi, K.; Yuk, H.; Floresca, H. C.; Kim, M. J.; Hu, W. *Nano Lett.* **2011**, *11*, 1412–1417.
- (5) Liu, B.; Wang, Y.; Ho, T.; Lew, K. -K.; Eichfeld, S. M.; Redwing, J. M.; Mayer, T. S.; Mohny, S. E.; *J. Vac. Sci. Technol. A*, **2008**, *26*(3)
- (6) Konagai, M. *JJAP* **2011**, *50*, 030001.
- (7) Wanekaya, A. K.; Chen, W.; Myung, N. V.; Mulchandani, A.; *Electroanalysis* **2006**, No. 6, 533–550.
- (8) Schmidt, V.; Wittemann, J. V.; Senz, S.; Gösele, U. *Adv. Mater.* **2009**, *21*, 2681–2702 and references therein.
- (9) Van de Walle, C. G.; Northrup, J. E. *Phys. Rev. Lett.* **1993**, *70*, 1117–1119.
- (10) Shir, D.; Liu, B. Z.; Mohammad, A. M.; Lew, K. K.; Mohny, S. E. *J. Vac. Sci. Technol. B* **2006**, *24*, 3.
- (11) Büttner, C. C.; Zacharias, M. *Appl. Phys. Lett.* **2006**, *89*, 263106 and references therein.
- (12) Liu, J. L.; Lu, Y.; Shi, Y.; Gu, S. L.; Jiang, R. L.; Wang, F.; Bu, H. M.; Zheng, R. L. *J. Phys. Status Solidi* **1998**, *168*, 441.
- (13) Bondi, R. J.; Lee, S.; Hwang, G. S. *ACS Nano* **2011**, *5*, 1713–1723.
- (14) Deal, B. E.; Grove, A. S. *J. Appl. Phys.* **1965**, *36*, 3770–3778.
- (15) Kao, D. -B.; McVittie, J. P.; Nix, W. D.; Saraswat, C. K. *IEEE Trans. Electron Devices* **1988**, *35*, 25–37.
- (16) Liu, H. I.; Biegelsen, D. K.; Johnson, N. M.; Ponce, F. A.; Pease, R. F. W. *J. Vac. Sci. Technol. B* **1993**, *11*, 6.
- (17) Dalla Torre, J.; Bocquet, J.-L.; Limoge, Y.; Crocombette, J.-P.; Adam, E.; Martin, G. *J. Appl. Phys.* **2002**, *92*, 2.
- (18) Fazzini, P.-F.; Bonafos, C.; Claverie, A.; Hubert, A.; Ernst, T.; Respaud, M. *J. Appl. Phys.* **2011**, *110*, 033524.
- (19) Chen, Y. Modeling of the Self-Limiting Oxidation for Nanofabrication of Si. In *Technical Proceedings of the Third International Conference on Modeling and Simulation of Microsystem*; San Diego, CA, March 27–29, 2000; Nano Science and Technology Institute: Austin, TX, 2000; pp 56–58.
- (20) van Duin, A. C. T.; Dasgupta, S.; Lorant, F.; Goddard, W. A., III. *J. Phys. Chem. A* **2001**, *105*, 9396–9409.
- (21) Abell, G. C. *Phys. Rev. B* **1985**, *31*, 6184–6196.
- (22) Mortier, W. J.; Ghosh, S. K.; Shankar, S. *J. Am. Chem. Soc.* **1986**, *108*, 4315–4320.
- (23) Buehler, M. J.; van Duin, A. C. T.; Goddard, W. A. *Phys. Rev. Lett.* **2006**, *96*, 095505.

- (24) Khalilov, U.; Neyts, E. C.; Pourtois, G.; van Duin, A. C. T. *J. Phys. Chem. C* **2011**, *115*, 24839–24848 and references therein.
- (25) van Duin, A. C. T.; Baas, J. M. A.; van de Graaf, B. *J. Chem. Soc., Faraday Trans.* **1994**, *90*, 2881–2895.
- (26) van Duin, A. C. T.; Strachan, A.; Stewman, S.; Zhang, Q.; Xu, X.; Goddard, W. A., III. *J. Phys. Chem. A* **2003**, *107*, 3803–3811.
- (27) Ning, N.; Calvo, F.; van Duin, A. C. T.; Wales, D. J.; Vach, H. *J. Phys. Chem. C* **2009**, *113*, 518–523.
- (28) Fogarty, J. C.; Aktulga, H. M.; Grama, A. Y.; van Duin, A. C. T.; Pandit, S. *J. Chem. Phys.* **2010**, *132*, 174704 and references therein.
- (29) Neyts, E. C.; Khalilov, U.; Pourtois, G.; van Duin, A. C. T. *J. Phys. Chem. C* **2011**, *115* (11), 4818–4823.
- (30) Neyts, E. C.; Shibuta, Y.; van Duin, A. C. T.; Bogaerts, A. *ACS Nano* **2010**, *4*, 6665–6672.
- (31) Neyts, E. C.; van Duin, A. C. T.; Bogaerts, A. *J. Am. Chem. Soc.* **2011**, *133*, 17225–17231.
- (32) Valentini, P.; Schwartzentruber, T. E.; Cozmuta, I. *J. Chem. Phys.* **2010**, *133*, 084703.
- (33) Mueller, J. E.; van Duin, A. C. T.; Goddard, W. A., III. *J. Phys. Chem. C* **2010**, *114*, 5675–5685.
- (34) Berendsen, H. J. C.; Postma, J. P. M.; van Gunsteren, W. F.; DiNola, A.; Haak, J. R. *J. Chem. Phys.* **1984**, *81* (8), 3684–3690.
- (35) Daruka, I.; Barabási, A.-L.; Zhou, S. J.; Germann, T. C.; Lomdahl, P. S.; Bishop, A. R. *Phys. Rev. B* **1999**, *60*, R2150–R2153.
- (36) Kato, K.; Uda, T.; Terakura, K. *Phys. Rev. Lett.* **1998**, *80*, 2000.
- (37) Orellana, W.; da Silva, A. J. R.; Fazzio, A. *Phys. Rev. Lett.* **2003**, *90*, 016103.
- (38) Choi, C. H.; Liu, D.; Evans, J. W.; Gordon, M. S. *J. Am. Chem. Soc.* **2002**, *124*, 8730–8740.
- (39) Cerofolini, G. F.; Mascolo, D.; Vlad, M. O. *J. Appl. Phys.* **2006**, *100*, 054308.
- (40) Stoneham, A. M.; Szymanski, M. A.; Shluger, A. L. *Phys. Rev. B* **2001**, *63*, 221304.
- (41) Pasquarello, A.; Hybertsen, M.; Car, R. *Appl. Surf. Sci.* **1996**, *104/105*, 317–322.
- (42) Mozzi, R. L.; Warren, B. E. *J. Appl. Crystallogr.* **1969**, *2*, 164–172.
- (43) Hamann, D. R. *J. Phys. Rev. Lett.* **1998**, *81*, 3447–3450.
- (44) Ng, K.-O.; Vanderbilt, D. *Phys. Rev. B* **1999**, *59*, 10132–10137.
- (45) Mauri, F.; Pasquarello, A.; Pfrommer, B. G.; Yoon, Y.-G.; Louie, S. G. *Phys. Rev. B* **2000**, *62*, 4786–4789.
- (46) Watanabe, T.; Tatsumura, K.; Ohdomari, I. *Appl. Surf. Sci.* **2004**, *237*, 125–133.
- (47) Da Silva, J.; Pinatti, D.; Anderson, C.; Rudee, M. *Philos. Mag.* **1975**, *31*, 713.